Fabrication of pyrimidine/g-C$_3$N$_4$ nanocomposites for efficient photocatalytic activity under visible-light illumination

Jingguo Zhuang[a,1], Jing Zhang[b,1], Jingyu Pang[a,*], Aijian Wang[b,**], Xinhai Wang[a,***], Weihua Zhu[b]

[a] Henan Engineering Research Center of Industrial Circulating Water Treatment, College of Chemistry and Chemical Engineering, Henan University, Kaifeng, 475004, PR China
[b] School of Chemistry & Chemical Engineering, Jiangsu University, Zhenjiang, 212013, PR China

ABSTRACT

In this work, a series of pyrimidine/g-C$_3$N$_4$ photocatalysts has been synthesized via a facile solvothermal method for the first time. The structure, elemental composition and morphology of the photocatalysts were characterized by FT-IR, SEM, XPS, N$_2$ adsorption-desorption isotherms and BET characterization methods. The photocatalytic activity of the pyrimidine/g-C$_3$N$_4$ materials was investigated by the degradation of rhodamine solution under visible-light illumination. The pyrimidine/g-C$_3$N$_4$ photocatalyst with 1 wt% of pyrimidine shows the highest photocatalytic activity for the degradation of RhB, which can be mainly ascribed to the effective interfacial charge transfer within the pyrimidine/g-C$_3$N$_4$ photocatalyst and the cooperation effect of the excellent contact interface between g-C$_3$N$_4$ and pyrimidine. The main active species during the photodegradation process are determined by the radical trapping experiments, proving that the superoxide radical ($\cdot$O$_2^-$) and the hydroxyl radical ($\cdot$OH) play the main role in the photocatalytic reactions.

1. Introduction

The environmental pollution is harmful to the living beings, so the development of new high efficiency technology for the pollutant control and pollutant elimination is necessary. In the past decades, the visible-light responsive semiconductor based photocatalysts have gained considerable interdisciplinary attention due to their potential environment applications and diverse potential in energy, and the design of visible-light-responsive photocatalyst is essential for the efficient utilization of the solar energy. To date, developing a high quality semiconductor photocatalyst has become a hot research area. Indeed, there were numerous visible-light-responsive photocatalysts that have been reported [1–6]. However, visible-light applications of these semiconductor photocatalysts are restricted for some limitations, such as the large band gap energy, high cost, and scarcity (especially noble metals) [7–11]. Therefore, the graphitic carbon nitride (g-C$_3$N$_4$) as one non-metal semiconductor has become a new star generation photocatalyst in the research communities.

Due to its appealing electronic structure with a suitable band gap ($\sim$2.7 eV), good chemical and thermal stability [12,13], g-C$_3$N$_4$ has attracted great interest as visible-light responded photocatalyst for water splitting and organic pollutants degradation (such as rhodamine B). However, the photocatalytic performance of g-C$_3$N$_4$ is severely limited by the small surface area, rapid recombination of photoinduced charge (electrons and holes). Recently, many research efforts have been devoted to enhance the photocatalytic efficiency of the g-C$_3$N$_4$ under visible-light irradiation, such as elements doping using the noble metal [14] or nonmetallic elements [15], coupling with other different semiconductors [16], and organic dye sensitization [17,18]. Among these various strategies for visible-light harvesting, organic dyes (e.g., metal-porphyrins [3], poly (3-hexylthiophene) [17] and Erythrosin B (ErB) [19]) have been widely used as photosensitizers due to its potential applications in the fields of optical device and photocatalysis. In particular, these dyes can dramatically extend the visible-light region of the wide band-gap semiconductors. The pyrimidine ring as a six-membered aromatic heterocycle with two nitrogen atoms is present in various optical active compounds. It is worth noting that the 4,6-distyrylpyrimidine derivatives have found various applications in our

---

daily life, i.e. organic semiconductors, visible-light harvesting system, and optoelectronic materials [20]. Particularly, the 4,6-distyrylpyrimidine as the scaffold has been used to design the push-pull structure for photonic materials [21]. However, to the best our knowledge, the pyrimidine derivatives modified g-C$_3$N$_4$ has never been reported until now.

In this work, we reported the preparation, characterization, optical property and photocatalytic performances of the pyrimidine/g-C$_3$N$_4$ nanocomposites by varying the contents of pyrimidine for the first time. The photocatalytic activity of the pyrimidine/g-C$_3$N$_4$ composites were investigated by the degradation of rhodamine B (RhB) solution under visible-light illumination. The pyrimidine/g-C$_3$N$_4$ photocatalyst with 1 wt% of pyrimidine shows the highest photocatalytic activity for the degradation of RhB, resulting from the strong interfacial interactions among the components. The optimal content of the pyrimidine for the photocatalytic performances was also determined based on the photocatalytic reaction kinetics acquiring from the degradation of RhB solution.

2. Experimental

2.1. Materials and reagents

RhB and dicyandiamide (C$_2$H$_4$N$_4$) are provided by Shanghai Sinopharm Chemical Reagent Co. Ltd, China. All other chemical reagents in this study are analytical grade and used without further purification. Distilled water is used in all of our experiments. The 4,6-bis(2-butoxy-4-(diethylamino)styryl) pyrimidine-2-ol (pyrimidine) was prepared according to a previous literature [22].

2.2. Synthesis of pyrimidine/g-C$_3$N$_4$ composites

The g-C$_3$N$_4$ was obtained by the pyrolysis of C$_2$H$_4$N$_4$ according to the reported method [23]. The pyrimidine/g-C$_3$N$_4$ composites were synthesized by a facile solvothermal technique. The g-C$_3$N$_4$ (40 mg) and a certain amount of pyrimidine were added into 25 mL tetrahydrofuran (THF), and subjected to ultrasound for 2 h to be completely dispersed, and then stirred for 4 h under reflux. After cooling down to room temperature, the solvent was removed by rotary evaporation, and then the obtained products were dried under vacuum at room temperature for 12 h. To study the influence of pyrimidine on the photocatalysis, the content of pyrimidine added into the pyrimidine/g-C$_3$N$_4$ materials is 0.5 wt%, 1 wt%, 2 wt%, 2.5 wt%, and 3 wt%, which are marked as PC0.5, PC1, PC2, PC2.5 and PC3, respectively.

2.3. Material characterization

The as-prepared pyrimidine/g-C$_3$N$_4$ composites were characterized by different techniques. Fourier Transform Infrared (FT-IR) spectra were obtained on a MB 154S-FTIR spectrophotometer (Bomen, Canada) using standard KBr pellet technique within the wavenumber range of 400–4000 cm^{-1}. The scanning electron microscopy (SEM, S4800, Hitachi Co., Japan) and transmission electron microscopy (TEM, JEOL, JEM-2010F) were used to investigate the morphologies of the as-prepared samples. The Brunauer-Emmett-Teller (BET) surface area of the as-prepared samples was measured on a NOVA 2000e instrument. The X-ray photoelectron spectroscopy (XPS) was taken on a RBD upgraded PHI−5000C ESCA (PerkinElmer) electron spectrometer with a monochromatic Mg Kα source, which was used to determine the composition of the samples. UV–Vis diffuse reflection spectroscopy (DRS) were registered on a Varian Cary 500 spectrophotometer within the range of 200–800 nm, and the BaSO$_4$ pellet was used as the reference at room temperature. The steady-state photoluminescence (PL) spectra were recorded with a Fluoro-Max-P spectrofluorimeter, and the excitation wavelengths were 337 and 400 nm. To study the photoinduced carrier behaviors of the samples, the photoelectrochemical tests including

transient photocurrent measurements and electrochemical impedance spectroscopy (EIS) measurements were measured on an electrochemical workstation (CHI 614D, CH Instrument). Both experiments were recorded using a classical three electrode quartz with 0.2 M Na$_2$SO$_4$ electrolyte solution.

2.4. Photodegradation experiments

The photocatalytic activity of the samples was investigated by the degradation of RhB in aqueous solution under visible-light irradiation supplied by a 350 W Xe-lamp with a 420 nm cut-off filter (Nanshen Company, Shanghai). All experiments were performed in a horizontal quartz tubular reactor (length = 28 cm, volume = 160 mL). A flat quartz plate was employed to hold the photocatalysts. In general, some catalyst (9 mg) was suspended in 30 mL RhB (1.5×10^{-5} mol/L) aqueous solution. In order to achieve the adsorption-desorption balance between the RhB and the photocatalyst surface, the suspension was stirred in the dark for 30 min. During the photocatalytic decolorization process, 3.0 mL of the reaction suspension was collected at certain time intervals under visible light irradiation. After each photocatalytic reaction, the catalyst was separated by centrifugation immediately. Concentrations of RhB at different conditions were analyzed by recording variations of the maximum absorption peak at 554 nm using a UV–vis spectrophotometer (UV-2450, Shimadzu). To investigate the role of the active species involved in the photocatalytic processes, and the trapping experiments were performed using different sacrificial agents.

3. Results and discussion

3.1. Structure, composition and morphology

In order to confirm the existence of pyrimidine in the as-prepared pyrimidine/g-C$_3$N$_4$ composites, the FT-IR spectra were recorded, and the results being shown in Fig. 1. For pure g-C$_3$N$_4$, there were five absorption peaks at 1643, 1564, 1441, 1325 and 1239 cm^{-1}, corresponding to the typical C−N heterocyclic stretching modes. The absorption band at 805 cm^{-1} is related to the characteristic breathing vibration of the tris-triazine rings [24–26]. In the case of the as-prepared composites, the characteristic peaks for g-C$_3$N$_4$ still remain. However, no characteristic peaks of pyrimidine can be observed in Fig. 1, which may be due to the low loadings of the pyrimidine in the as-prepared composites.

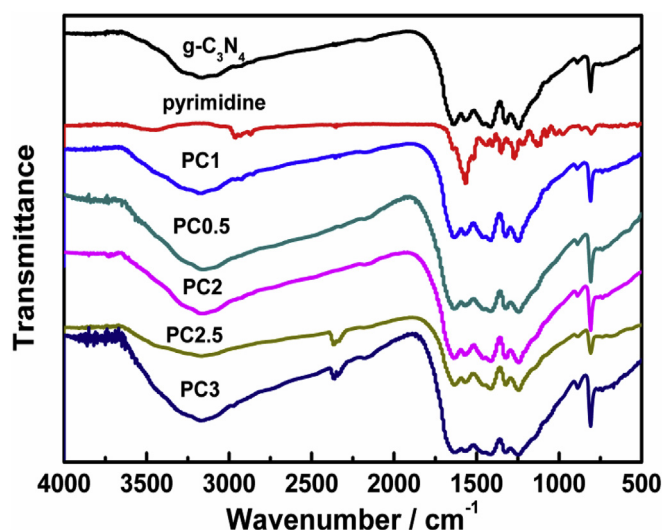The SEM images of the as-synthesized g-C$_3$N$_4$, pyrimidine, and PC1

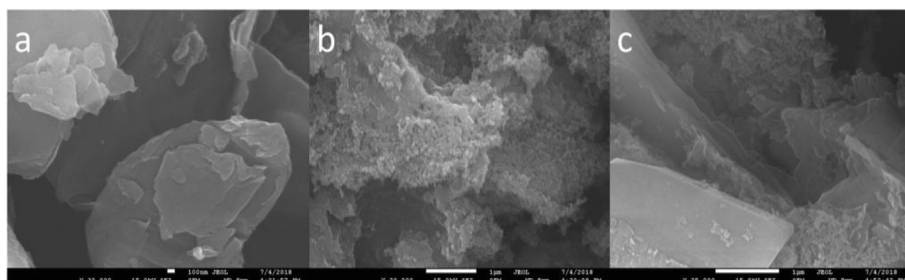**Fig. 1.** FT-IR spectra of the as-prepared samples.

Fig. 2. SEM images of (a) g-C_3N_4, (b) pyrimidine, and (c) PC1.

were shown in Fig. 2. It can be seen that the g-C_3N_4 exhibits a lamellar structure of agglomerates with a size of several micrometers (Fig. 2a). The pyrimidine reveals a large quantity of irregular sheetlike porous structure (Fig. 2b). After coupling with g-C_3N_4, significant structural and morphological changes were observed for PC1 (Fig. 2c), implying that the pyrimidine was successfully loaded onto the surface of g-C_3N_4. The TEM images (Fig. S1 in Supporting Information) also confirmed that the pyrimidine/g-C_3N_4 samples were synthesized successfully [24]. The introduction of pyrimidine significantly modified the morphology structure of the g-C_3N_4, further creating massively intrinsic channels for photogenerated holes and electrons due to the π-π interactions between g-C_3N_4 and pyrimidine, which may lead to improved photodegradation efficiency.

To further study the specific surface area and porosity, which were considered as important factors for photocatalysis, the N_2 adsorption and desorption measurement were performed. As shown in Fig. 3, the pure g-C_3N_4 and PC1 composite exhibit a typical IV isotherm, suggesting that the existence of mesoporosity structure. The Brunauer-Emmett-Teller (BET) surface area per unit mass of PC1 composite is $10.412 \, m^2 \, g^{-1}$, and the total pore volume is $0.072 \, cm^3 \, g^{-1}$, which is larger than that of pure g-C_3N_4 ($7.954 \, m^2 \, g^{-1}$ and $0.065 \, cm^3 \, g^{-1}$). Although the surface area of PC1 is larger than that of g-C_3N_4, it is even smaller when compared to other reported values [15,18]. Accordingly, the increased surface in the present case may not play the main role for the higher photocatalytic activity.

The XPS measurements were used to further study the chemical components and the surface state of the as-prepared samples (Fig. 4). The survey spectrum of the pyrimidine and PC1 were shown in Fig. 4a, it can be found that the existence of C, N, and O elements in the PC1 composite, consistent with the chemical composition of the composite material. Fig. 4b shows the N 1s spectrum of pure g-C_3N_4. Three peaks located at approximately 398.37, 398.98 and 400.34 eV are observed

for g-C_3N_4. The peak at 398.37 eV can be ascribed to the C=N−C sp²-bonded nitrogen unit. The peak at 398.98 eV corresponds to the tertiary nitrogen N-$(C)_3$ group, while the peak observed at 400.34 eV is assigned to the secondary amino group C−N−H [27–29]. As shown in Fig. 4c, the N 1s spectra of the pyrimidine exhibits two peaks at 398.61 and 400.02 eV, which is assigned to the N species in the C−N and C=N bonds, respectively [30]. However, an obvious blue shift was observed for the N 1s peaks of PC1 composite when compared to pure g-C_3N_4 (400.32, 398.32, and 398.96 eV). The C 1s spectrum of g-C_3N_4 (Fig. S2a) shows three peaks located at 284.68, 287.93 and 288.46 eV, corresponding to the adventitious carbon, C=N bonds and C−N or C-$(N)_3$ groups. The C 1s spectrum of pyrimidine demonstrates five peaks at 283.82, 284.26, 284.59, 285.07, and 285.8 eV in Fig. S2b. For PC1, five peaks located at 284.18, 284.67, 285.18, 287.86 and 288.4 eV were observed due to the hybridization of g-C_3N_4 with pyrimidine (Fig. S2c). Similarly, a red-shift was also found for the O 1s spectrum of PC1 when compared to pyrimidine (Fig. S3). These shift may be caused by the interfacial interactions between the pyrimidine and pure g-C_3N_4, which played an important role in promoting the transfer of photogenerated electrons (e−) and holes (h+) within the photocatalyst [31].

3.2. Optical and photoelectrochemical properties

The optical characterization of pyrimidine/g-C_3N_4 nanocomposites was examined by the UV–vis diffuse reflectance spectra (DRS) and PL spectroscopy measurements. From the UV–vis absorption spectra (Fig. 5a), the pure g-C_3N_4 exhibited a typical intrinsic absorption at around 470 nm [32]. After the introduction of pyrimidine, the absorption edge of the PC1 showed a significantly enhanced background absorption through the entire UV–vis region. Furthermore, a broad visible light wave-band absorption is observed for PC1 composite, which may be due to the pure pyrimidine possesses the high absorption coefficient in the visible light region and/or the π-π stacking between g-C_3N_4 and pyrimidine. It is recognized that the PC1 composite can be excited more easily to promote photogenerated electron-hole pairs, and then enhance the photocatalytic performance under visible light [33,34]. The PL spectra was further employed to analyze the efficiency of charge transfer and recombination of photogenerated electrons (e−) and holes (h+) of the as-prepared samples. Fig. 5b shows the PL spectra of the pure g-C_3N_4 and PC1 nanocomposite under the excitation wavelength of 377 nm. The pure g-C_3N_4 exhibits a strong PL emission peak centered at around 462 nm because of the n-π* electronic transitions, suggesting more recombination of photogenerated hole and electron pairs on the surface of g-C_3N_4 [35]. However, the PC1 exhibits an obviously blue-shift and significant fluorescence quenching due to the presence of pyrimidine. Many researches indicated that lower photoluminescence intensity signified higher separation efficiency of charge and electron-hole pairs, implying that the radiative recombination of photogenerated electrons (e−) and holes (h+) is largely inhibited due to the introduction of pyrimidine [36]. A similar result is observed for g-C_3N_4 and PC1 upon excitation at 337 nm, the results being shown in Fig. S4. Furthermore, to understand well the charge transfer dynamics properties of the g-C_3N_4 and PC1, the time-resolved PL decay spectra

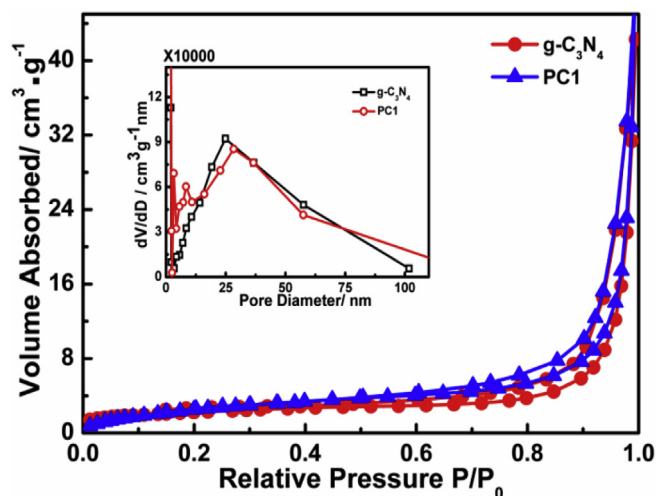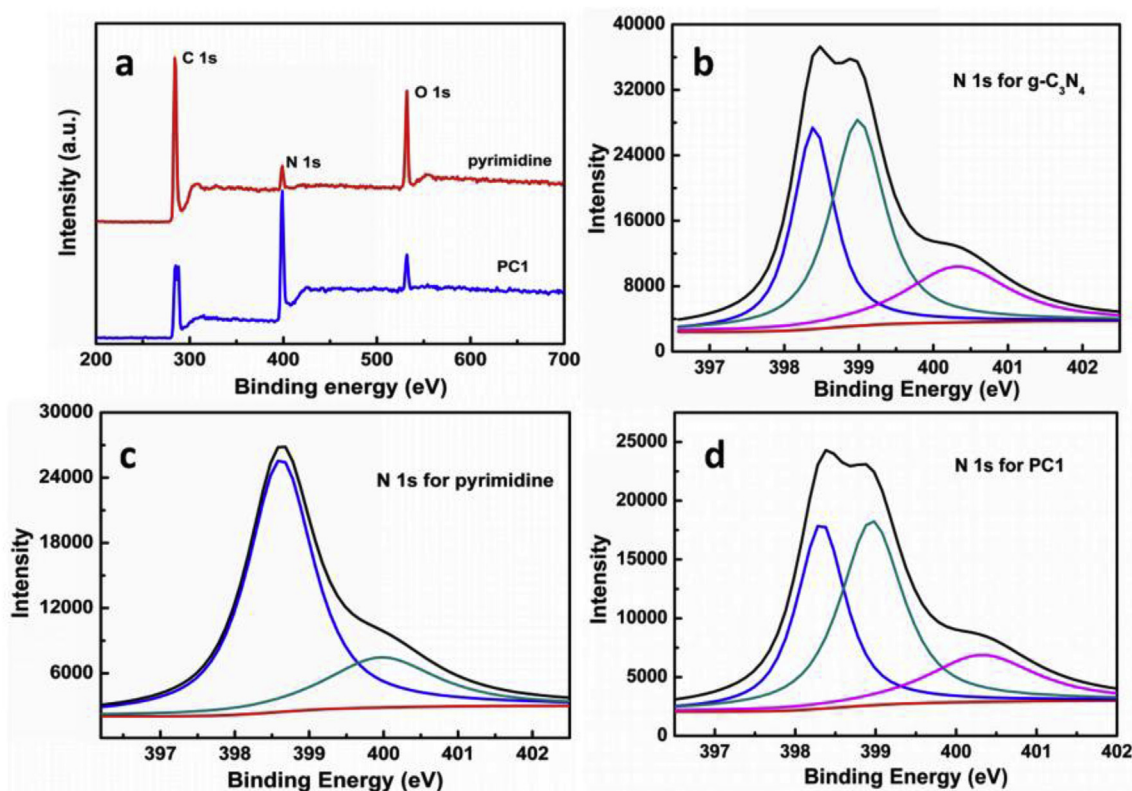**Fig. 3.** Nitrogen adsorption-desorption isotherms of g-C_3N_4 and PC1 composite.

Fig. 4. (a) XPS patterns of the pyrimidine and the PC1 composite. High resolution XPS spectra: N 1s of (b) g-C$_3$N$_4$, (c) pyrimidine, and (d) PC1.

(Fig. S5) was recorded. The lifetime of the pure g-C$_3$N$_4$ and PC1 is determined to be 0.87 and 5.69 ns, respectively. This result illustrated that the introduction of pyrimidine can efficiently promote the separation of the electron-hole pairs [37].

Based on the above experimental results, it is believed that the charge separation and migration play a significant effect on the photocatalytic activity of semiconductor materials [31]. In order to better understand the interfacial charge separation and transfer dynamics of g-C$_3$N$_4$ and PC1 materials under the visible-light irradiation, the transient photocurrent responses and EIS measurements were employed. Fig. 6a displays the photocurrent-time (I-t) curves of g-C$_3$N$_4$ and PC1 upon the visible-light irradiation. When the lamp was turned on, the photocurrent responses of the working electrodes increased sharply and then reached a stable value, originating from the fast separation of the

photoinduced charge carriers. In contrast, when the lamp was turned off, the photocurrent rapidly decreased to initial status, and maintains its dark current state. As shown in Fig. 6a, the PC1 composite exhibits a higher transient photocurrent response than pure g-C$_3$N$_4$, which implies that the decrease of the photoinduced electrons and holes recombination, and thus the lifetime of the electron-hole pairs are extended effectively. Furthermore, the photoinduced charge transfer behaviors were also studied by the EIS experiments. Fig. 6b shows the EIS results of g-C$_3$N$_4$ and PC1 composite. The EIS arc radius of PC1 is significantly decreased in comparison with that of pure g-C$_3$N$_4$. Hence, the introduction of pyrimidine can greatly enhance the absorption wavelength region and significantly improve the charge separation efficiency, leading to high photocatalytic and photoelectric activity [38].
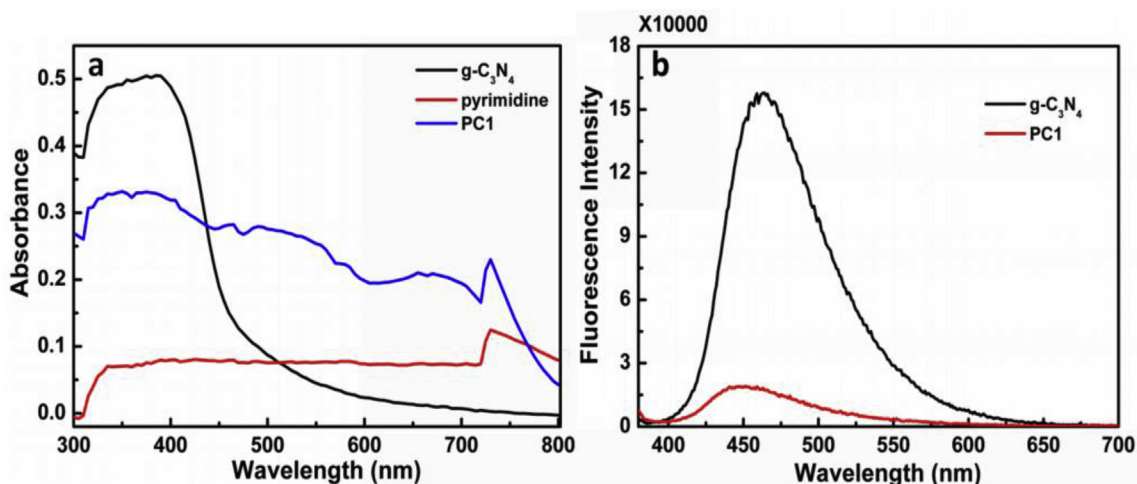

Fig. 5. (a) UV–Vis diffuse reflectance spectra of g-C$_3$N$_4$, pyrimidine, and PC1. (b) Steady-state photoluminescence spectra of g-C$_3$N$_4$ and PC1.
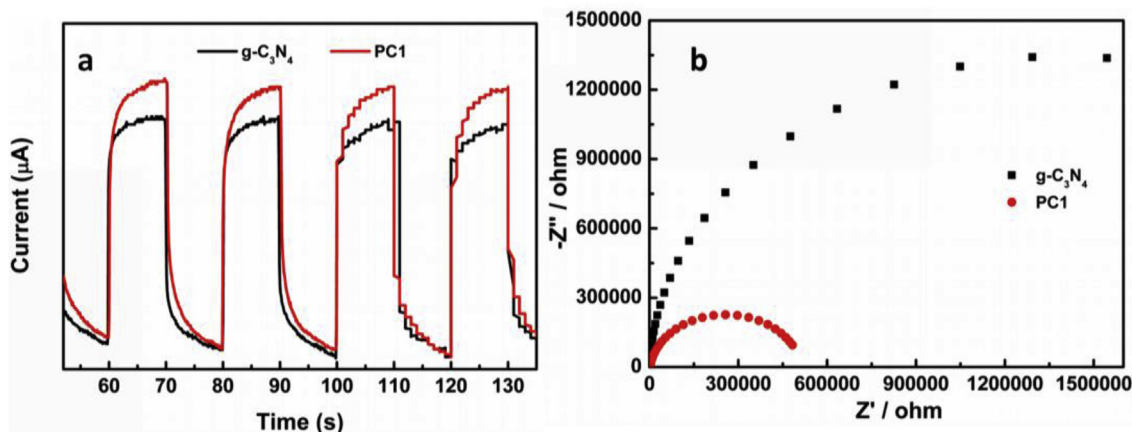
Fig. 6. (a) Transient photocurrent responses and (b) EIS spectra of g-C$_3$N$_4$ and PC1 composite.

3.3. Photocatalytic performance

The photocatalytic performance of the pure g-C$_3$N$_4$, pyrimidine and the as-fabricated pyrimidine/g-C$_3$N$_4$ photocatalysts was assessed by the degradation of RhB solution under visible-light illumination. As depicted in Fig. 7a, the contents of pyrimidine play an important effect on the photocatalytic performance of the pyrimidine/g-C$_3$N$_4$ photocatalysts. The PC0.5, PC1 and PC2 exhibited an enhanced photodegradation efficiency of RhB. Moreover, the PC1 composite showed the highest photocatalytic activity for the degradation of RhB solution with a degradation rate of 92.1%, while only 61.5% and 25.9% of RhB were degraded for pure g-C$_3$N$_4$ and pyrimidine within 135 min. Unfortunately, when the content of pyrimidine further increased (> 2.0%), the photocatalytic activity of the photocatalyst declined gradually, which clearly suggest that the content of pyrimidine plays a

great influence on the photocatalytic activity of the pyrimidine/g-C$_3$N$_4$ composites. Too much pyrimidine on the surface of the g-C$_3$N$_4$ may shield the g-C$_3$N$_4$ from absorbing visible light, then the lower light harvesting caused a detrimental influence on the photogeneration of electron-hole pairs, leading to the declined photocatalytic activity of pyrimidine/g-C$_3$N$_4$ composites [39,40]. To quantitatively investigate the photocatalytic reaction kinetics of the photocatalysts, the pseudo-first-order kinetics model: ln (C/C$_0$) = kt were used, where k (min^{-1}) represents the rate constant, C$_0$ (mg/L) is the original concentration of RhB, and C (mg/L) represents the concentration at illumination time t. Fig. 7b shows the calculated k values of the as-synthesized samples for the photodegradation of RhB, it shows that the PC1 composite exhibits the maximum rate constant (k = 0.024 min^{-1}), which is about 2.67 times higher than the pure g-C$_3$N$_4$ (k = 0.009 min^{-1}).

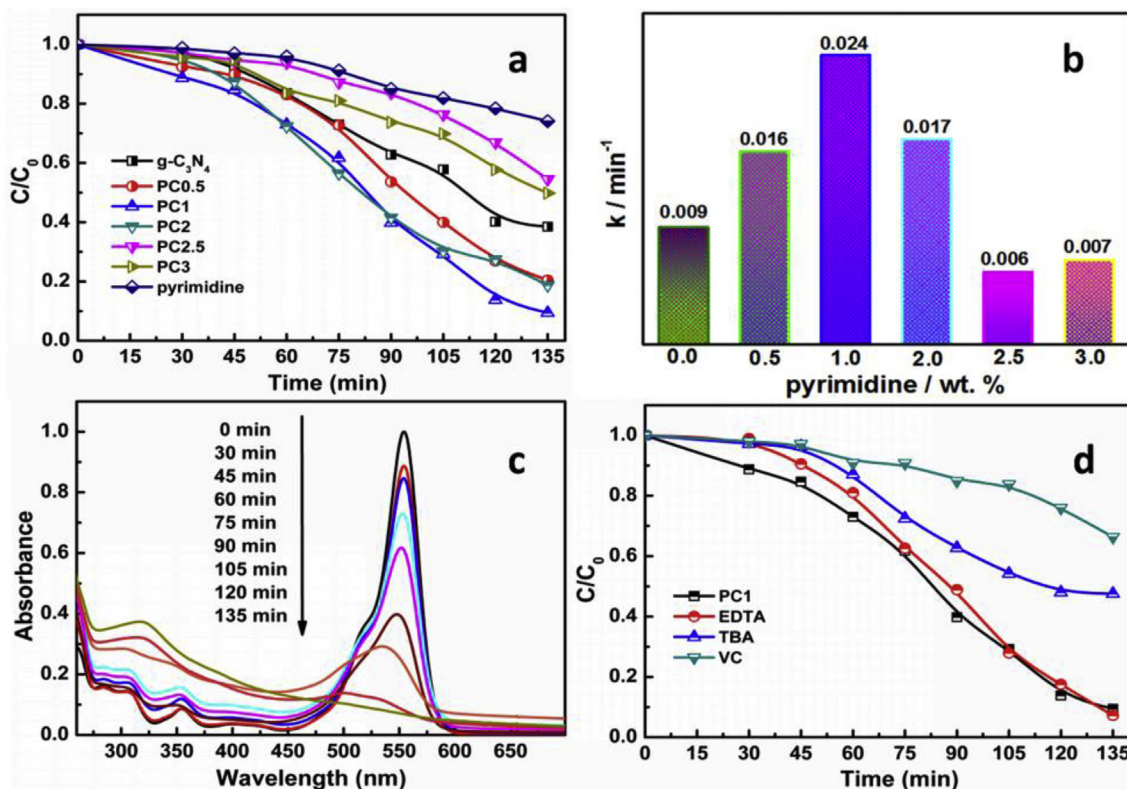In order to study the photocatalytic efficiency of PC1 more

Fig. 7. (a) Photocatalytic degradation of the as-fabricated samples for the RhB solutions; (b) The kinetic constants of the different photocatalysts; (c) UV–vis spectral changes of RhB solutions during the photodegradation by PC1; (d) Trapping experiments of active species in the system for the degradation of RhB solutions by PC1.

Fig. 8. Photodegradation mechanism for the RhB solution by the pyrimidine/g-C₃N₄ composites under visible-light irradiation.

intuitively, the time-resolved UV–vis absorption spectra of RhB solution in the presence of PC1 was recorded in Fig. 7c. It can be found that during the photodegradation process, the main absorption peak of RhB at λ = 554 nm decreases gradually as the irradiation time increases. Meanwhile, the color changes from initial pink to colorless after 135 min visible light irradiation, which indicate that the PC1 can make the RhB completely decolorization. Moreover, a blue shift of the absorption peak of RhB is also observed with the irradiation time increases, resulting from the formation of the N-deethylation and N-demethylation [41]. This results indicates that the RhB dye can be degraded by the as-fabricated photocatalyst.

It is important to investigate the active species in the photocatalytic process to understand well the degradation mechanism. Thus in this study, we used three different scavengers, i.e. TBA, EDTA-2Na, and VC to quench the •OH, h⁺ and •O₂⁻, respectively. As shown in Fig. 7d, when the EDTA-2Na was added into the degradation system, the PC1 showed the highest photocatalytic activity for the degradation of RhB solution, revealing that the h⁺ is not the main active radical in this photodegradation process. However, when the TBA and VC were added into the system, the degradation rates were decreased to be 52.44% and 33.68%, respectively, revealing that the •O₂⁻ and •OH should be the main active radicals in the photodegradation process [42–45]. In addition, the decreased degree of degradation rate upon addition of VC is larger than that upon addition of TBA, implying that the •O₂⁻ plays a more important role than the •OH in the RhB photodegradation process.

Based on the DRS, EIS, PL analysis and radical trapping experiments, a possible photodegradation mechanism for degradation of RhB solution by the pyrimidine/g-C₃N₄ composites was presented in Fig. 8. Upon the visible light irradiation, the photoexcited electrons would transfer from the valence band (VB) of the pyrimidine to the conduction band (CB), and then transfer to the CB of g-C₃N₄. At the same time, these electrons can be trapped by the O₂ near the surface of the composites to generate •O₂⁻. The excess •O₂⁻ may further take part in the reaction to form •OH radicals [46], both of them can degrade the RhB solutions. The experimental results, including PL, photocurrent and EIS spectra, suggest that the introduction of pyrimidine is favorable for the interfacial charge transfer, which can decrease the photoinduced electron-hole recombination, resulting in the improved photocatalytic performance.

4. Conclusions

In this work, the pyrimidine/g-C₃N₄ photocatalysts have been synthesized via a facile solvothermal method for the first time. The structure, elemental composition and morphology of the photocatalysts were characterized by FT-IR, SEM, XPS, N₂ adsorption-desorption isotherms and BET characterization methods. The PC1 composite with 1 wt% of pyrimidine shows the highest photocatalytic activity for the degradation of RhB solution with a degradation rate of 92.1%. The experimental results suggest that the introduction of pyrimidine can promote the interfacial charge transfer and decrease the photoinduced electron-hole recombination, which is benefit to the photocatalytic performance.

This result provides new insights into the design of g–C₃N₄–based photocatalysts with good performances.

Appendix A. Supplementary data

Supplementary data to this article can be found online at https://doi.org/10.1016/j.dyepig.2018.12.046.

References

[1] Ong W-J, Tan L-L, Ng YH, Yong S-T, Chai S-P. Graphitic carbon nitride (g-C₃N₄)-based photocatalysts for artificial photosynthesis and environmental remediation: are we a step closer to achieving sustainability? Chem Rev 2016;116:7159–329.
[2] Chen Z, Yu X, Zhu QH, Fan TT, Wu QL, Zhang LZ, Li JH, Fang WP, Yi XD. Steam engraving optimization of graphitic carbon nitride with enhanced photocatalytic hydrogen evolution. Carbon 2018;139:189–94.
[3] Zhang J, Wang AJ, Zhao W, Li C, Chen XD, Wang Y, Zhu WH, Zhong Q. Influence of metal-porphyrins on the photocatalysis of graphitic carbon nitride. Dyes Pigments 2018;153:241–7.
[4] Di J, Xia JM, Chen XL, Ji MX, Yin S, Zhang Q, Li HM. Tunable oxygen activation induced by oxygen defects in nitrogen doped carbon quantum dots for sustainable boosting photocatalysis. Carbon 2016;114:601–7.
[5] Chen P, Wang F, Chen ZF, Zhang QX, Su YH, Shen LZ, Yao K, Liu Y, Cai ZW, Lv WY, Liu GG. Study on the photocatalytic mechanism and detoxicity of gemfibrozil by a sunlight-driven TiO₂/carbon dots photocatalyst: the significant roles of reactive oxygen species. Appl Catal, B 2017;204:250–9.
[6] Tu WG, Zhou Y, Zou ZG. Versatile graphene-promoting photocatalytic performance of semiconductors: basic principles, synthesis, solar energy conversion, and environmental applications. Adv Funct Mater 2013;23:4996–5008.
[7] Jourshabani M, Shariatinia Z, Achari G, Langford CH, Badiei A. Facile synthesis of NiS₂ nanoparticles ingrained in a sulfur-doped carbon nitride framework with enhanced visible light photocatalytic activity: two functional roles of thiourea. J Mater Chem A 2018;6:13448–66.
[8] Zhou KG, McManus D, Prestat E, Zhong X, Shin Y, Zhang HL, Haigh SJ, Casiraghi C. Self-catalytic membrane photo-reactor made of carbon nitride nanosheets. J Mater Chem A 2016;4(30):11666–71.
[9] Chen P, Wang FL, Zhang QX, Su YH, Shen LZ, Yao K, Chen ZF, Liu Y, Cai ZW, Lv WY, Liu GG. Photocatalytic degradation of clofibric acid by g-C₃N₄/P25 composites under simulated sunlight irradiation: the significant effects of reactive species. Chemosphere 2017;172:193–200.
[10] Zhao W, Wang AJ, Wang Y, Lv CC, Zhu WH, Dou SP, Wang Q, Zhong Q. Accessible fabrication and mechanism insight of heterostructured BiOCl₆/Bi₂MoO₆/g-C₃N₄ nanocomposites with efficient photosensitized activity. J Alloy Comp 2017;726:164–72.
[11] Wang FL, Chen P, Feng YP, Xie ZJ, Liu Y, Su YH, Zhang QX, Wang YF, Yao K, Lv WY, Liu GG. Facile synthesis of N-doped carbon dots/g-C₃N₄ photocatalyst with enhanced visible-light photocatalytic activity for the degradation of indomethacin. Appl Catal, B 2017;207:103–13.
[12] Zhang QX, Chen P, Tan CW, Chen TS, Zhuo MH, Xie ZJ, Wang FL, Liu HG, Cai ZW, Liu GG, Lv WY. A photocatalytic degradation strategy of PPCPs by a heptazine-based CN organic polymer (OCN) under visible light. Environ Sci: Nano 2018;5(10):2325–36.
[13] Sun ZC, Zhu MS, Fujitsuka M, Wang AJ, Shi C, Majima T. Phase effect of NiₓPᵧ hybridized with g-C₃N₄ for photocatalytic hydrogen generation. ACS Appl Mater Interfaces 2017;9(36):30583–90.
[14] Sun BW, Li HJ, Yu HY, Qian DJ, Chen M. In situ synthesis of polymetallic Co-doped g-C₃N₄ photocatalyst with increased defect sites and superior charge Carrier properties. Carbon 2017;117:1–11.
[15] Ke L, Li PF, Wu X, Jiang SJ, Luo MB, Liu YH, Le ZG, Sun CZ, Song SP. Graphene-like sulfur-doped g-C₃N₄ for photocatalytic reduction elimination of UO₂²⁺ under visible light. Appl Catal, B 2017;205:319–26.
[16] Ji MX, Di J, Ge YP, Xia JX, Li HM. 2D-2D stacking of graphene-like g-C₃N₄/ultrathin Bi₄O₅Br₂ with matched energy band structure towards tntibiotic removal. Appl Surf Sci 2017;413:372–80.
[17] Yan HJ, Huang Y. Polymer composites of carbon nitride and poly(3-hexylthiophene) to achieve enhanced hydrogen production from water under visible light. Chem Commun 2011;47(14):4168–70.
[18] Chen DM, Wang KW, Hong WZ, Zong RL, Yao WQ, Zhu YF. Visible light photoactivity enhancement via CuTCPP hybridized g-C₃N₄ nanocomposite. Appl Catal, B 2015;166–167:366–73.
[19] Wang YB, Hong JD, Zhang W, Xu R. Carbon nitride nanosheets for photocatalytic hydrogen evolution: remarkably enhanced activity by dye sensitization. Catal. Sci.

Technol. 2013;3(7):1703–11.

[20] Achelle S, Plé N. Pyrimidine ring as building block for the synthesis of functionalized π-conjugated materials. Curr Org Synth 2012;9:163–87.

[21] Achelle S, Rodríguez-López, Guen FR. Photoluminescence properties of aryl-, arylvinyl-, and arylethynylpyrimidine derivatives. ChemistrySelect 2018;3:1852–86.

[22] Liu Z, Chen T, Liu B, Huang ZL, Huang T, Li S, Xu Y, Qin J. Two-photon absorption of a series of V-shape molecules: the influence of acceptor's strength on two-photon absorption in a noncentrosymmetric D-π-A-π-D system. J Mater Chem C 2007;17:4685–9.

[23] Fu YS, Zhu JW, Hu C, Wu XD, Wang X. Covalently coupled hybrid of graphitic carbon nitride with reduced graphene oxide as a superior performance lithium-ion battery anode. Nanoscale 2014;6(21):12555–64.

[24] Xia JX, Zhao JZ, Chen J, Di J, Ji MX, Xu L, Chen ZG, Li HM. Facile fabrication of g-C₃N₄/BiPO₄ hybrid materials via a reactable ionic liquid for the photocatalytic degradation of antibiotic ciprofloxacin. J Photochem Photobiol, A 2017;339:59–66.

[25] Wang X, Hong MZ, Zhang FW, Zhuang ZY, Yu Y. Recyclable nanoscale zero valent Iron doped g-C₃N₄/MoS₂ for efficient photocatalysis of RhB and Cr(VI) driven by visible light. ACS Sustainable Chem Eng 2016;4(7):4055–63.

[26] Zheng Y, Lin LH, Ye XJ, Guo FS, Wang XC. Helical graphitic carbon nitrides with photocatalytic and optical activities. Angew Chem Int Ed 2014;53(44):11926–30.

[27] Vattikuti SVP, Byon C. Hydrothermally synthesized ternary heterostructured MoS₂/Al₂O₃/g-C₃N₄ photocatalyst. Mater Res Bull 2017;96:233–45.

[28] Cui LF, Liu YF, Wang YT, Fang XY, Yin CC, Kang SF, Dong MD. Constructing ultrathin g-C₃N₄ nanosheets with hierarchical pores by NaClO induced wet etching for efficient photocatalytic Cr(VI) detoxification under visible light irradiation. Diam Relat Mater 2018;88:51–9.

[29] Ge L, Zuo F, Liu JK, Ma Q, Wang C, Sun DZ, Bartels L, Feng PY. Synthesis and efficient visible light photocatalytic hydrogen evolution of polymeric g-C₃N₄ coupled with CdS quantum dots. J Phys Chem C 2012;116(25):13708–14.

[30] Zhu JH, Li YX, Chen Y, Wang J, Zhang B, Zhang JJ, Blau WJ. Graphene oxide covalently functionalized with zinc phthalocyanine for broadband optical limiting. Carbon 2011;49(6):1900–5.

[31] Wang AJ, Zhang J, Zhao W, Zhu WH, Zhong Q. Porphyrin decorated Bi₂O₂CO₃ nanocomposites with efficient difunctional properties of photocatalysis and optical nonlinearity. J Alloy Comp 2018;748:929–37.

[32] Wang JJ, Tang L, Zeng G, Liu Y, Zhou Y, Deng Y. Plasmonic Bi metal deposition and g-C₃N₄ coating on Bi₂WO₆ microspheres for efficient visible light photocatalysis. ACS Sustainable Chem Eng 2017;5(1):1062–72.

[33] Zhao W, Li C, Wang AJ, Lv CC, Zhu WH, Dou SP, Wang Q, Zhong Q. Polyaniline decorated Bi₂MoO₆ nanosheets with effective interfacial charge transfer as photocatalysts and optical limiters. Phys Chem Chem Phys 2017;19(42):28696–709.

[34] Chen YF, Huang WX, He DL, Situ Y, Huang H. Construction of heterostructured g-C₃N₄/Ag/TiO₂ microspheres with enhanced photocatalysis performance under visible-light irradiation. ACS Appl Mater Interfaces 2014;6(16):14405–14.

[35] Zhang Z, Wu S, Zhang J, Tang SX, Hu CY, Li YG, Jiang LN, Cui QL. Well-aligned carbon nitride nanorods: the template-free synthesis and their optical and thermal properties. Appl Phys A 2015;119:1507–13.

[36] Li ML, Zhang LX, Wu MY, Du YY, Fan XQ, Wang M, Zhang LL, Kong QL, Shi JL. Mesostructured CeO₂/g-C₃N₄ nanocomposites: remarkably enhanced photocatalytic activity for CO₂, reduction by mutual component activations. Nanomater Energy 2016;19:145–55.

[37] Zhang QX, Chen P, Zhuo MH, Wang FL, Su YH, Chen TS, Yao K, Cai ZW, Lv WY, Liu GG. Degradation of indometacin by simulated sunlight activated CDs-loaded BiPO4, photocatalyst: roles of oxidative species. Appl Catal, B 2018;221:129–39.

[38] Wang ZY, Huang Y, Ho WK, Cao JJ, Shen ZX, Lee SC. Fabrication of Bi₂O₂CO₃/g-C₃N₄ heterojunctions for efficiently photocatalytic NO in air removal: in-situ self-sacrificial synthesis, characterizations and mechanistic study. Appl Catal, B 2016;199:123–33.

[39] Di J, Xia JX, Ji MX, Xu L, Yin S, Zhang Q, Chen ZG, Li HM. Carbon quantum dots in situ coupling to bismuth oxyiodide via reactable ionic liquid with enhanced photocatalytic molecular oxygen activation performance. Carbon 2016;98:613–23.

[40] Xia JX, Ji MX, Di J, Wang B, Yin S, Zhang Q, He MQ, Li HM. Construction of ultrathin C₃N₄/Bi₄O₅I₂ layered nanojunctions via ionic liquid with enhanced photocatalytic performance and mechanism insight. Appl Catal, B 2016;191:235–45.

[41] Liu CY, Huang HW, Du X, Zhang TR, Tian N, Guo YX, Zhang YH. In situ Co-crystallization for fabrication of g-C₃N₄/Bi₅O₇I heterojunction for enhanced visible-light photocatalysis. J Phys Chem C 2015;119(30):17156–65.

[42] Li W, Tian Y, Zhao C, Zhang Q, Geng W. Synthesis of magnetically separable Fe₃O₄@PANI/TiO₂ photocatalyst with fast charge migration for photodegradation of EDTA under visible-light irradiation. Chem Eng J 2016;303:282–91.

[43] Sun M, Li SL, Yan T, Ji PG, Zhao X, Yuan K, Wei D, Du B. Fabrication of heterostructured Bi₂O₂CO3/Bi₂O₄ photocatalyst and efficient photodegradation of organic contaminants under visible-light. J Hazard Mater 2017;333:169–78.

[44] Shan W, Hu Y, Bai Z, Zheng M, Wei C. In situ preparation of g-C₃N₄/bismuth-based oxide nanocomposites with enhanced photocatalytic activity. Appl Catal, B 2016;188:1–12.

[45] Ji MX, Liu YL, Di J, Chen R, Chen ZG, Xia JX, Li HM. N-CQDs accelerating surface charge transfer of Bi₄O₅I₂ hollow nanotubes with broad spectrum photocatalytic activity. Appl Catal, B 2018;237:1033–43.

[46] Song X, Hu Y, Zheng MM, Wei CH. Solvent-free in situ synthesis of g-C₃N₄/{001}TiO₂ composite with enhanced UV- and visible-light photocatalytic activity for NO oxidation. Appl Catal, B 2016;182(5):587–97.